Applied Catalysis B: Environmental 258 (2019) 117984

Contents lists available at ScienceDirect

Applied Catalysis B: Environmental

journal homepage: www.elsevier.com/locate/apcatb

Double-catalytic-site engineering of nickel-based electrocatalysts by group VB metals doping coupling with in-situ cathodic activation for hydrogen evolution

Xiao Shang[a], Xin-Yu Zhang[a], Jing-Yi Xie[a,b], Bin Dong[a,b,*], Jing-Qi Chi[a], Bao-Yu Guo[a,b], Min Yang[a], Yong-Ming Chai[a,**], Chen-Guang Liu[a]

[a] State Key Laboratory of Heavy Oil Processing, Institute of New Energy, China University of Petroleum (East China), Qingdao 266580, PR China
[b] College of Science, China University of Petroleum (East China), Qingdao 266580, PR China

ARTICLE INFO

Keywords:
Double-site catalysis
Group VB transition metal
In-situ cathodic activation
Coupling strategy
Alkaline hydrogen evolution

ABSTRACT

The hydrogen evolution reaction (HER) in alkaline media is limited by poor-proton environment with the water dissociation step. Herein, we report a double-catalytic-site construction strategy for nickel-based materials (e.g., sulfides, selenides, phosphides and oxides) for HER, utilizing group VB metals (V, Nb or Ta) doping coupled with the subsequent in-situ cathodic activation (ICA). For V-doped nickel sulfide, ICA creates Ni–V oxides species as new active sites for water dissociation. Moreover, V dopants enhance the intrinsic activity of nickel sulfide by the electronic interaction between Ni and V during the ICA process. As a result, the double-catalytic-site system composed of Ni–V sulfides-oxides hybrid achieves 4-fold higher intrinsic activity and 15-fold larger current density at the overpotential of 300 mV than those of pristine nickel sulfide. Our work may open up a new avenue for designing multi-site systems, which may be promisingly applied for other transition metal materials in the electrolysis field.

1. Introduction

Electrocatalysis are promising technologies to convert intermittent renewable energies (solar or wind) into high-value chemicals [1,2]. Hydrogen evolution reaction (HER) of water electrolysis is especially crucial to provide hydrogen product as an important clean energy carrier and raw material for industrial process [3]. The sluggish kinetics in HER process critically necessitate efficient electrocatalysts, however, the most active noble Pt-based materials cannot be widely employed due to the scarcity and high cost [4,5]. It is thus highly desirable to develop non-precious alternatives for water splitting.

In view of the thermodynamic convenience for the oxygen evolution reaction in high pH conditions, the alkaline electrolyte is highly preferred in industrial hydrogen production [6]. One main obstacle that remained unresolved in alkaline HER is the poor-proton electrolysis environment causing additional water dissociation step and energy barriers [7,8]. Towards this issue, it is highly advocated to construct double-site catalysis system where each site facilitates one certain reaction step and synergistically improves the catalysis performance [9,10]. For example, the $Ni(OH)_2$ in $Ni(OH)_2$/Pt catalyst promotes the water dissociation while the Pt sites are responsible for combining H intermediates into hydrogen molecular [11]. Many similar structures have been explored to construct the bifunctional catalyst, such as Ni $(OH)_2/Ni_3S_2$ [12], NiO/Ni-CNT [13], CoMn-S@NiO [14], Ni-MoS_2 [15], Ni/NiO/$CoSe_2$ [16] and so on. However, these syntheses may be limited to a small range of electrocatalysts. Besides, the intrinsic activity of each active site is expected to be modulated in terms of the electronic structure or interfaces engineering, such as metal doping or creating heterostructures [17,18]. Few studies have ever focused on the double-site catalysis system modification because of the challenges of simultaneous tailoring on each site. Recently, the in-situ electrochemical activation in atmosphere condition emerges as a novel activation pretreatment on electrocatalysts [19–22]. These processes have successfully realized the simultaneous structural engineering and electronic tuning [23,24]. Their controllable manipulation, convenience and environmental friendliness features are attractive to be applied for modifying the double-site catalysis system for alkaline HER.

Herein, we have designed a double-catalytic-site construction

* Corresponding author at: State Key Laboratory of Heavy Oil Processing, Institute of New Energy, China University of Petroleum (East China), Qingdao 266580, PR China.
** Corresponding author.
E-mail addresses: dongbin@upc.edu.cn (B. Dong), ymchai@upc.edu.cn (Y.-M. Chai).

https://doi.org/10.1016/j.apcatb.2019.117984
Received 20 March 2019; Received in revised form 15 July 2019; Accepted 21 July 2019
Available online 23 July 2019
0926-3373/

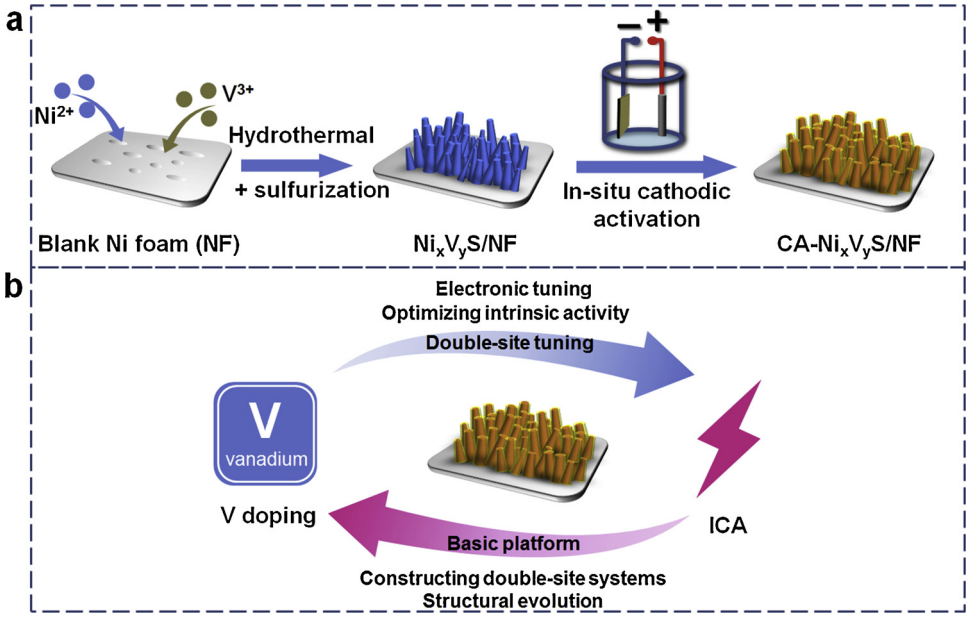

Scheme 1. (a) Synthesis procedure for V doped nickel sulfide (Ni_xV_yS/NF) followed by ICA pretreatment (CA-Ni_xV_yS/NF). (b) Brief scheme of coupling interaction between V doping and ICA pretreatments.

strategy on nickel-based materials by coupling group VB metals (V, Nb or Ta) doping with the subsequent in-situ cathodic activation (ICA). The synthesis procedure is illustrated in Scheme 1a with V-doped nickel sulfide as the example. The Ni–V bimetallic sulfide nanoclusters on porous Ni foam with high surface areas provide great versatility for modification during electrochemical activation. Then the ICA process induces the generation of bimetallic Ni–V oxides covering on surfaces to form oxide-sulfide hybrids as the double-site catalysis system.

Furthermore, it reveals a strong coupling interaction between V doping and ICA as briefly described in Scheme 1b. The ICA process constructs the basic metal oxide-sulfide hybrids as double-site catalysis system. The V doping facilitates the ICA process to generate more metal oxide-sulfide double sites. Moreover, the V dopants also improve the intrinsic activity of nickel sulfide by the electron interaction between Ni and V during ICA. As a result, the in-situ formed bimetallic oxides accelerate the water dissociation step, while the activated nickel sulfide promotes the recombination of H intermediates in alkaline HER. Moreover, the coupling strategies are proved to be versatile on other group VB metals (Nb and Ta) as well as other nickel derivatives (selenides, phosphides and oxides) for efficient alkaline HER.

2. Experimental

All chemical reagents were of analytical grade and were used as received without further purification. Nickel foam (NF) with thickness of 1.0 mm was purchased from Shenzhen Poxon Machinery Technology Co. Ltd.

Prior to the synthesis, NF (1 × 2 cm^2) was sonicated in acid, acetone and ethanol consecutively for 30 min, followed by drying in vacuum at 60 °C. In the typical synthesis of Ni_xV_yO/NF, $NiCl_2{\cdot}6H_2O$ and VCl_3 with different Ni/V ratios of 1:0, 9:1, 1:3, and 1:9 were mixed in 50 mL of deionized water containing 3 mmol of urea. The total amount of Ni and V ions was fixed to 2 mmol. The clean NF with the above solution was transferred into an autoclave (100 mL) at 120 °C for 12 h, followed by calcination in air at 400 °C for 2 h with heating rate of 1 °C min^{-1}. The final products were denoted as NiO/NF, $Ni_{0.9}V_{0.1}O$/NF, $Ni_{0.25}V_{0.75}O$/NF and $Ni_{0.1}V_{0.9}O$/NF, respectively. The in-situ cathodic activation (ICA) of as-prepared samples was carried out by a typical three-electrode system (Gamry Reference 600 Instruments, USA) in 1.0 M KOH electrolyte (protected by N_2 atmosphere). The as-prepared sample was used as the working electrode, and a saturated calomel electrode (SCE) and a graphite rod (length of 50 mm, diameter of 3 mm) were used as the reference and counter electrode, respectively. The ICA was performed by consecutive linear sweep voltammetry (LSV) from −1.0 to −1.9 V (vs. SCE) with the scan rate of 10 mV s^{-1} until reaching a stable HER activity. The ICA-treated samples of NiO/NF and $Ni_{0.25}V_{0.75}O$/NF above were denoted as CA-NiO/NF and CA-$Ni_{0.25}V_{0.75}O$/NF, respectively.

In the typical synthesis of Ni_xV_yS/NF, the as-prepared Ni_xV_yO/NF was sulfurized in H_2S/N_2 gas (volume ratio of 1/9) at 300 °C for 2 h with heating rate of 3 °C min^{-1} to obtain the final product of NiS/NF, $Ni_{0.9}V_{0.1}S$/NF, $Ni_{0.25}V_{0.75}S$/NF and $Ni_{0.1}V_{0.9}S$/NF, respectively, corresponding to Ni/V source ratios of 1:0, 9:1, 1:3 and 1:9. For comparison, the vanadium sulfide supported by Ti foil (VS/Ti foil) was prepared in the similar sulfurization process without the addition of Ni source. The ICA-treated sample of VS/Ti foil and Ni_xV_yS/NF above were denoted as CA-VS/Ti foil and CA-Ni_xV_yS/NF, respectively.

In the typical synthesis of $Ni_{0.25}Nb_{0.75}O$/NF, $NiCl_2{\cdot}6H_2O$ and $NbCl_5$ with Ni/Nb ratio of 1/3 (total amount of 2 mmol) were dissolved in 25 mL of ethanol and then added by 25 mL of deionized water. Then the clean NF with the above solution was transferred into an autoclave (100 mL) at 180 °C for 24 h. After cooling down to room temperature, the product was carefully rinsed with deionized water and ethanol, followed by drying in vacuum at 60 °C. The preparation of $Ni_{0.25}Ta_{0.75}O$/NF was under similar condition with $TaCl_5$ as Ta source. The synthesis of $Ni_{0.25}Nb_{0.75}S$/NF and $Ni_{0.25}Ta_{0.75}S$/NF were similar with Ni_xV_yS/NF. The ICA-treated samples of $Ni_{0.25}Nb_{0.75}S$/NF and $Ni_{0.25}Ta_{0.75}S$/NF were denoted as CA-$Ni_{0.25}Nb_{0.75}S$/NF and CA-$Ni_{0.25}Ta_{0.75}S$/NF, respectively.

In the typical synthesis of $Ni_{0.25}V_{0.75}P$/NF, the as-prepared $Ni_{0.25}V_{0.75}O$/NF was placed at the center of a tube furnace and 1.0 g of $NaH_2PO_2{\cdot}H_2O$ was placed at the upstream side. The center of the furnace was elevated to 400 °C with a heating rate of 3 °C min^{-1}. The preparation of $Ni_{0.25}V_{0.75}Se$/NF was under similar conditions by using Se powder (1.0 g) as Se source. The ICA-treated samples of $Ni_{0.25}V_{0.75}P$/NF and $Ni_{0.25}V_{0.75}Se$/NF were denoted as CA-$Ni_{0.25}V_{0.75}P$/NF and CA-$Ni_{0.25}V_{0.75}Se$/NF, respectively.

The electrochemical measurements to evaluate the electrocatalytic performances of the above electrocatalysts were undertaken in the three-electrode system (Gamry Reference 600 Instruments, USA). The

as-prepared sample was utilized as the working electrode, with a saturated calomel electrode and a graphite rod as the reference and counter electrode, respectively. The electrolyte was the fresh 1.0 M KOH electrolyte and was protected by N_2 gas during the measurement. Linear sweep voltammetry (LSV) was conducted from −1.0 V to −1.9 V (vs. SCE) with the scan rate of 5 mV s^{-1}. Electrochemical impedance spectroscopy (EIS) was performed at −1.18 V (vs. SCE) with the frequency from 10^5 to 10^{-2} Hz and an AC voltage of 5 mV. The double-layer capacitance (C_{dl}) of electrocatalyst was estimated by cyclic voltammogram (CV) at the potential window from −0.9 to −1.1 V (vs. SCE) in different scan rates (40, 60, 80, 100 and 120 mV s^{-1}). The detailed calculation method was shown in the supporting information. The stabilities were estimated by chronoamperometry (i − t) at −1.3 V (vs. SCE) or CV (−1.0 to −1.6 V vs. SCE). The electrochemical data were presented with iR (current times internal resistance) correction. The potentials conversion from SCE to reversible hydrogen electrode (RHE) is based on the equation as follows [25]:

$$E\ (\text{vs. RHE}) = E\ (\text{vs. SCE}) + 0.244\ \text{V} + (0.059\ \text{V})\ \text{pH} = E\ (\text{vs. SCE}) + 1.05\ \text{V}$$

X-ray diffraction (XRD) patterns were obtained on X'Pert PRO MPD diffractometer (Cu Kα). Scanning electron microscopy (SEM) images were undertaken on Hitachi S-4800 instrument. X-ray fluorescence elemental analysis (EDX) was conducted over a representative area of sample. X-ray photoelectron spectra (XPS) were performed on ThermoFisher Scientific II spectrometer with Al as photo source. Transmission electron microscopy (TEM) and high-resolution transmission electron microscopy (HRTEM) images were acquired on FEI Tecnai G2. The inductively coupled plasma optical emission spectrometry (ICP-OES) was carried out on Shidmadzu ICPE-9000. The generated hydrogen gas was detected on a gas chromatograph system (SP6800A).

3. Results and discussion

In the first synthesis step, the initial catalysts of NiS/NF and $Ni_{0.25}V_{0.75}S$/NF were transformed from Ni-based oxide precursors in H_2S atmosphere at 300 °C. The XRD patterns (Fig. S1a) reveal the Ni_3S_2 hexagonal phase (PDF no. 01-073-0698) formed on NiS/NF and $Ni_{0.25}V_{0.75}S$/NF. It implies that the V doping does not introduce new crystalline phase and V dopants are amorphous. This may be due to the low content (0.82 wt%) of V element as proved by inductively coupled plasma optical emission spectrometry (ICP-OES) (Table S1). The surfaces on NiS/NF (Fig. S2a,b) and $Ni_{0.25}V_{0.75}S$/NF (Figs. S3a, 1 a,b, and S4) are composed of randomly-oriented nanoclusters in scanning electron microscopy (SEM) and transmission electron microscopy (TEM) images. The local region of nanoclusters on $Ni_{0.25}V_{0.75}S$/NF in HRTEM image (Fig. 1c) exhibits lattice fringes of 0.4, 0.28 and 0.23 nm corresponding to (101), (110) and (021) crystallographic planes of Ni_3S_2 phase. The related elemental mapping (Fig. S5) confirms that V element has doped into clusters and all elements are in uniform distribution. The above results suggest that the V doping maintains the Ni_3S_2 crystalline phase and the nanocluster morphology. Moreover, such homogeneous metal hybrids are supposed to efficiently facilitate the modulation of the electronic and chemical states of the catalyst surfaces than those of the heterogeneous metal-based hybrids [26].

In the subsequent tuning step of the in-situ cathodic activation (ICA), the Ni_3S_2 phase is maintained (Fig. S1) with the decreased the crystalline degree (Table S2), suggesting the surface amorphization on catalysts. Correspondingly, the roughened surfaces are observed on CA-NiS/NF (Fig. S2c,d) are suggested to be nickel oxide according to EDX mapping result (Fig. S6). The V doping even induced the formation of large amount of nanosheets (Fig. 1d,e) composed of Ni, V and O elements (Fig. S7), suggesting the in-situ generated Ni–V oxides by ICA. The inner nanocluster (Fig. 1f) structure of CA-$Ni_{0.25}V_{0.75}S$/NF still contains similar lattice fringe distances from Ni_3S_2 phase and is composed of uniform Ni, V and S elements (Fig. S8). The above results suggest that the ICA induces the formation of metal oxide-sulfide hybrids, and the coupled V doping promotes the construction of bimetallic oxide-sulfide hybrid structure.

The chemical changes of main elements after the coupled tuning strategies have been studied by X-ray photoelectron spectroscopy (XPS). The V doping did not cause the binding energy shift in Ni 2p spectra (Fig. S9a) of $Ni_{0.25}V_{0.75}S$/NF, which are still comprised of Ni(0) (852.7 and 873.4 eV), Ni—S (855.5 and 870.1 eV) and Ni—O (876.1 and 857.2 eV) species similar with NiS/NF (Fig. S10a) [27–29]. The V dopants are composed of V(IV) (516.2 and 523.1 eV) and V(V) (517.1 and 525.1 eV) species (Fig. 2c) [30]. Through ICA process, the binding energies of Ni-S and Ni(0) species in Ni 2p spectra of CA-$Ni_{0.25}V_{0.75}S$/NF are negatively shifted (Fig. 2b), in contrast to the unchangeable states of Ni species in CA-NiS/NF (Fig. 2a). Meanwhile, the peaks in V 2p region are all positively shifted to higher binding energies (Fig. 2c). The V doping did not influence the chemical state of sulfur (Fig. S9b) such as Ni—S bond (162.36 and 161.4 eV) [31] and V—S bond (163.44 eV) [32]. Note that the emerged SO_4^{2-} species (168.6 eV) on $Ni_{0.25}V_{0.75}S$/NF may be due to the sulfur oxidation in air. The above results suggest a strong electron interaction between V and Ni elements. As a consequence, the Ni sites in nickel sulfide are suggested to optimize the H intermediate adsorption and become more active for HER [12,23,33,34].

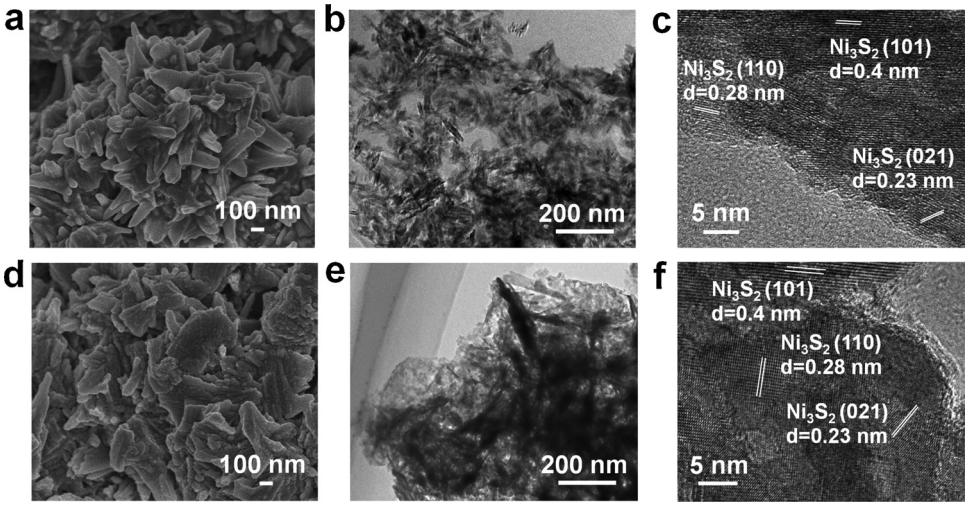

Fig. 1. (a) SEM, (b) TEM and (c) HRTEM images of $Ni_{0.25}V_{0.75}S$/NF. (d) SEM, (e) TEM and (f) HRTEM images of CA-$Ni_{0.25}V_{0.75}S$/NF.

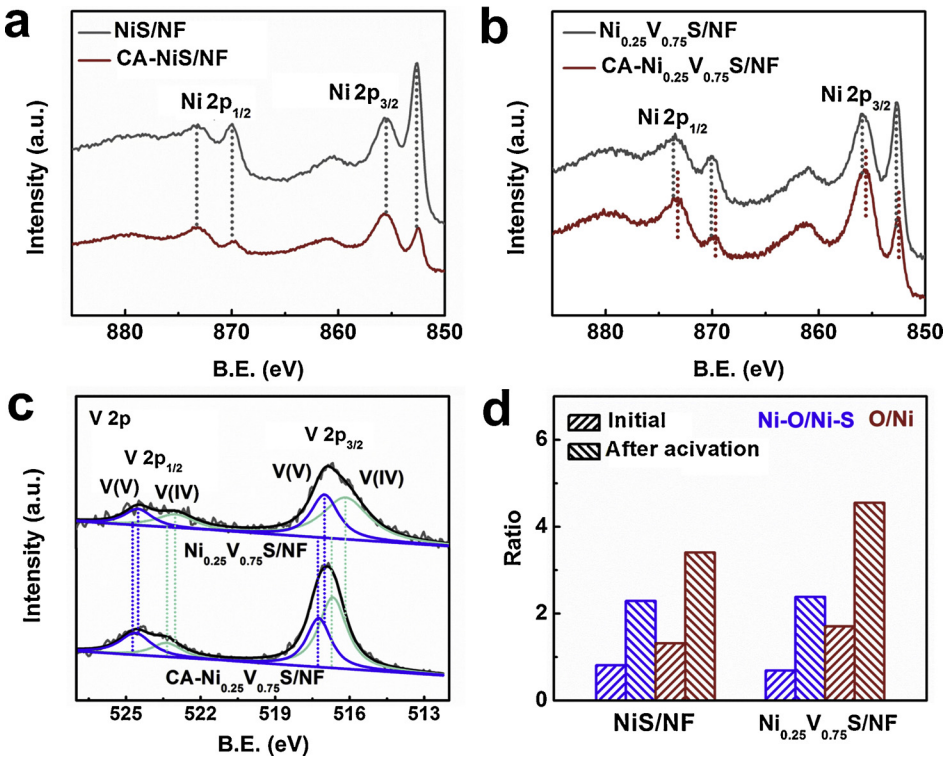

Fig. 2. High-resolution XPS spectra before and after activation. Ni 2p spectra of (a) NiS/NF and (b) $Ni_{0.25}V_{0.75}S$/NF. (c) V 2p spectra of $Ni_{0.25}V_{0.75}S$/NF. (d) Ni-O/Ni-S bond ratio before and after electrochemical activation.

Besides, the Ni—O/Ni—S bond ratios increase in both CA-NiS/NF and CA-$Ni_{0.25}V_{0.75}S$/NF (Tables S3, S4), confirming the generated metal oxides species by ICA. The sulfur mainly presents in the form of S^{2-} (Fig. S10c) rather than sulfur oxides, but the contents are obviously decreased (Tables S5, S6) for CA-NiS/NF and CA-$Ni_{0.25}V_{0.75}S$/NF. The formation of metal oxides in the reductive circumstance of electrochemical activation may be explained by favorable combination with oxygen than hydrogen atoms on transition metals [35,36]. Therefore, it can be concluded that the structural evolution induced by ICA involves the desulfurization on surfaces along with the formation of metal oxides [36]. The V doping especially facilitates the above processes to construct the bimetallic metal oxide-sulfide hybrid structure as the new catalysis interfaces. The resulted structural and electronic modifications by coupled tuning strategies are supposed to offer possibilities to modify the catalytic performances.

The electrocatalytic HER activities correlated with coupled tuning strategies are studied in 1.0 M KOH. For comparison, the two strategies are individually investigated to figure out their respective influences on catalysts. Under the overpotential of 300 mV, the polarization curves (Fig. 3a) present that the current densities of NiS/NF, CA-NiS/NF, $Ni_{0.25}V_{0.75}S$/NF and CA-$Ni_{0.25}V_{0.75}S$/NF are 8.6, 40, 8.8 and 133 mA cm^{-2}, respectively. This indicates the successful activation by the ICA to create the newly-formed double-catalytic-site system. However, the mere V doping strategy negligibly improves the HER activities without ICA process. Note that the separated vanadium sulfide species supported on Ti foil (denoted as VS/Ti foil) (Fig. S11) failed to be activated by ICA (denoted as CA-VS/Ti foil). Therefore the ICA mainly modifies the nickel sulfide structure rather than the V species. The above data indicate the higher activity of bimetallic oxide-sulfide catalysis system likely due to the synergistic effects between metal oxides and sulfides.

The HER activities are further investigated by other electrochemical measurements. The Tafel values (Fig. 3b) provide the information of possible catalytic reaction path or the rate limiting step (RLS). The Tafel slopes of NiS/NF and CA-NiS/NF are 189 and 128 mV dec^{-1}, respectively, suggesting that the related RLSs are Volmer reactions where protons are adsorbed to yield absorbed H intermediates [37]. The decreased Tafel slope of CA-NiS/NF means faster reaction kinetics in RLS process. The similar Tafel slope (184 mV dec^{-1}) of $Ni_{0.25}V_{0.75}S$/NF with that of NiS/NF illustrates that the mere V doping strategy cannot promote the RLS process. Once coupled with ICA treatment, the Tafel slope of CA-$Ni_{0.25}V_{0.75}S$/NF is notably decreased to 101 mV dec^{-1}, suggesting the evident change of RLS to Volmer-Heyrovsky process, involving the proton-participated electrochemical recombination [37]. It indicates that the bimetallic oxide-sulfide double site catalysis system can efficiently facilitate the water dissociation step [30]. The turnover frequency (TOF) is also measured to reveal the intrinsic activity changes. At the overpotential of 300 mV, the TOF values (Fig. 3c) of NiS/NF, CA-NiS/NF, $Ni_{0.25}V_{0.75}S$/NF and CA-$Ni_{0.25}V_{0.75}S$/NF are calculated to be −0.007, −0.015, −0.007 and −0.03 s^{-1}, respectively. This again confirms that the coupled tuning strategy can efficiently enhance the intrinsic HER activity. In addition, the Nyquist plots (Fig. 3d) reveal that the coupled tuning strategy also effectively decreases the electrochemical resistance of CA-$Ni_{0.25}V_{0.75}S$/NF for faster electron transportation in HER process. The insertion presents an equivalent circuit model including R_s (solution resistance), R_{ct} (charge transfer resistance) and CPE (constant phase angle element) [38]. The value of R_{ct} reflects the charge transfer process during the electrochemical reaction [39]. According to the fitting results (Table S7), CA-$Ni_{0.25}V_{0.75}S$/NF exhibits the smallest R_{ct} value (7.2 Ω) than $Ni_{0.25}V_{0.75}S$/NF (162.4 Ω), NiS/NF (206.6 Ω) and CA-NiS/NF (38.2 Ω), indicating that the charge transportation is notably improved on surfaces of CA-$Ni_{0.25}V_{0.75}S$/NF. Furthermore, in order to determine the Faradaic efficiency of HER, the measured amount of H_2 over CA-$Ni_{0.25}V_{0.75}S$/NF was compared with the theoretical value based on the charge transferred. As shown in Fig. S13, the actual amount of detected H_2 was correlated with the theoretical value and resulted in nearly 100% Faradaic efficiency. It indicates that the observed catalytic current over CA-$Ni_{0.25}V_{0.75}S$/NF originates only from the HER process.

The structural evolution and electronic modulation are further

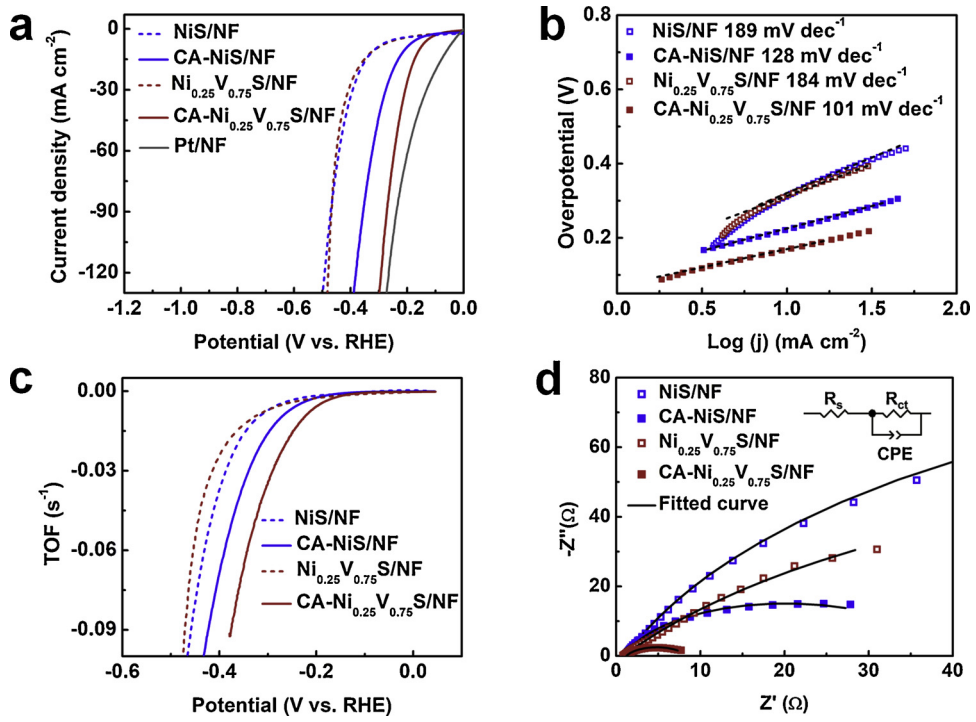

Fig. 3. HER performances of NiS/NF, CA-NiS/NF, $Ni_{0.25}V_{0.75}S$/NF and CA-$Ni_{0.25}V_{0.75}S$/NF in 1.0 M KOH. (a) HER polarization curves, (b) Tafel plots, (c) TOF and (d) Nyquist plots.

discussed. Based on the previous XPS results, it is speculated that metallic Ni may be generated for higher catalysis efficiencies [23,34]. To verify this proposal, the CV was conducted in 1.0 M KOH on anodic region (Fig. S14a). The redox peaks of Ni(II)/Ni(III) at 1.4–1.8 V (vs. RHE) are identified in pristine NiS/NF and $Ni_{0.25}V_{0.75}S$/NF. During the first anodic scan after ICA, the emerged oxidation peaks at 0.3–0.6 V (vs. RHE) represent the oxidation from Ni(0) to Ni(II) [34,40,41]. The larger oxidation peak of CA-$Ni_{0.25}V_{0.75}S$/NF than that of CA-NiS/NF obviously indicates more generated metallic Ni as active species created by the strong coupled tuning strategies. In addition, Raman spectra (Fig. S14b) were employed to study the bonding states of S-H_{ads} intermediate on catalysts. Prior to the electrochemical activation, no peak can be detected on NiS/NF and $Ni_{0.25}V_{0.75}S$/NF except for the Ni_3S_2 signals from 129 to 490 cm^{-1} [42]. After ICA, the S—H_{ads} bonds emerge at about 2550 cm^{-1} in CA-NiS/NF [43] and are shifted to 2500 cm^{-1} for CA-$Ni_{0.25}V_{0.75}S$/NF. This illustrates that the V dopants weaken the S—H_{ads} bonds on the surface, which is favorable for the hydrogen desorption [44].

All the physical and electrochemical results demonstrate the successful modification of the coupled strategies of ICA and V doping on nickel sulfide for efficient alkaline HER. The improving mechanism can be ascribed to the resulted bimetallic oxide-sulfide as double-site-catalytic system as illustrated in Fig. 4. The related explanations could be as following. (1) The initial nanostructures are the important prerequisite for the subsequent modulation and the finally high catalysis efficiency. The self-supported nanoclusters on conductive, porous three-dimensional (3D) Ni foam substrate possess high surface area and enhance the accessibility of active sites, as well as facilitates the mass/electron transportation [45–47]. Such advantageous framework also supplies flexible room for designing double-catalytic-site system [48]. (2) In the resulted double-catalytic-site system, the created bimetallic Ni–V oxides dramatically accelerate the water dissociation step in alkaline HER to offer more intermediate H for the subsequent step [13]. (3) In the other part of the double-catalytic-site system, the inner bimetallic Ni–V sulfides possess higher intrinsic activity in combining intermediate H to generate hydrogen molecule. (4) The close contact between the double catalytic sites, along with the electrical connection to the metallic current collector of Ni foam, ensures the excellent conductivity and the fast electron transportation in HER process [47,49].

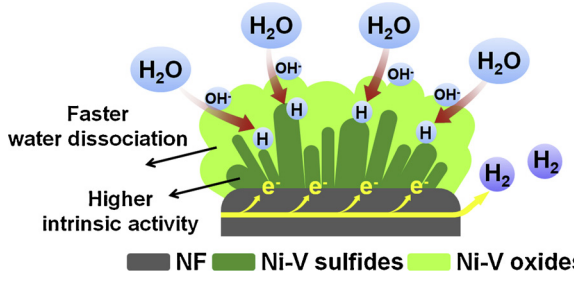

Fig. 4. Schematic illustration of bimetallic oxide-sulfide on $Ni_{0.25}V_{0.75}S$/NF as the double-catalytic-site catalyst in alkaline HER.

The coupling strategies are further optimized by changing the V doping degree. The different Ni/V molar ratios in precursor (9/1 and 1/9) are designed to prepare $Ni_{0.9}V_{0.1}S$/NF and $Ni_{0.1}V_{0.9}S$/NF, respectively. The increased V precursors result in larger V contents (Table S1) in catalysts. The coupled strategies retained the Ni_3S_2 phase (Fig. 5a) and the nanocluster morphology (Fig. S15). As reflected in XPS data, the chemical states of Ni species (Fig. S16a) are reduced for CA-$Ni_{0.9}V_{0.1}S$/NF, but remain unchangeable on CA-$Ni_{0.1}V_{0.9}S$/NF (Fig. S16b). This implies that the excessive V dopants fail to induce electronic modification and in turn impact the catalytic properties. In the related electrochemical measurements, the HER activities (Fig. S17a) increase from CA-$Ni_{0.9}V_{0.1}S$/NF to CA-$Ni_{0.25}V_{0.75}S$/NF, and then decrease for CA-$Ni_{0.1}V_{0.9}S$/NF, presenting the optimized Ni/V precursor ratio of 1/3. Correspondingly, the CA-$Ni_{0.25}V_{0.75}S$/NF exhibits the largest current density (123 mA cm^{-2}) and the highest TOF value (-0.03 s^{-1}) at the overpotential of 300 mV (Fig. 5b). The excellent HER performance of CA-$Ni_{0.25}V_{0.75}S$/NF can also be supported by the largest C_{dl} value (71.6 m F) (Fig. S18 and Table S8) and the smallest electrochemical resistance (Fig. S17c). The excellent HER activity of CA-

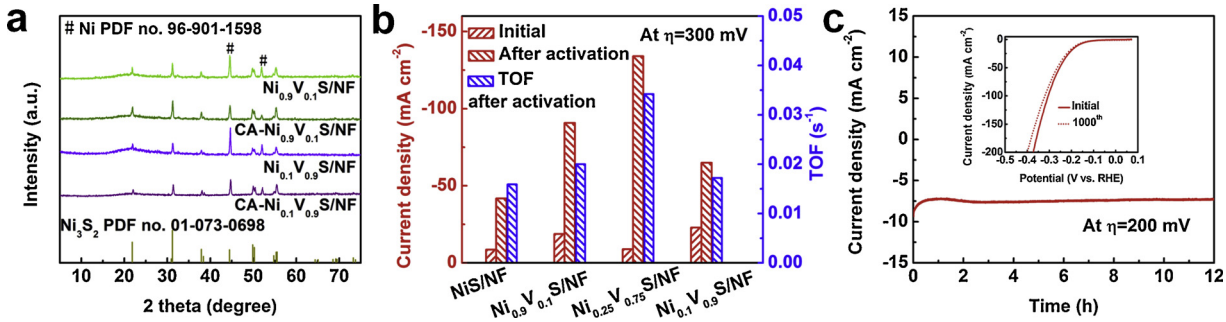

Fig. 5. (a) XRD patterns of $Ni_{0.9}V_{0.1}S$/NF, CA-$Ni_{0.9}V_{0.1}S$/NF, $Ni_{0.1}V_{0.9}S$/NF and CA-$Ni_{0.1}V_{0.9}S$/NF. (b) Comparison of the current densities and TOF at the overpotential of 300 mV. (c) Stability test of CA-$Ni_{0.25}V_{0.75}S$/NF by chronopotentiometry at the overpotential of 200 mV for 12 h. (Inset: stability test by potential cycling).

$Ni_{0.25}V_{0.75}S$/NF is comparable to many recent reports (Table S9). More importantly, CA-$Ni_{0.25}V_{0.75}S$/NF can maintain the excellent performance for at least 12 h at the constant overpotential of 200 mV (Fig. 5c). The long-term catalysis stability can also be reflected by the negligibly shifted polarization curve after consecutive CVs for 1000 cycles (Fig. 5c, inset). Afterwards, the well retained crystalline phase (Fig. S19a), chemical states (Fig. S19b,c) of main elements and nanoclusters (Fig. S20) confirm the structural stability of the double-catalytic-site system to ensure the lifespan of catalysts.

As in the same group VB, the Nb and Ta metals with the similar electronic structure are also supposed to activate the nickel sulfide through ICA. Herein the Nb- or Ta-doped nickel sulfide is synthesized based on the optimal Ni/V precursor ratio and are denoted as $Ni_{0.25}Nb_{0.75}S$/NF and $Ni_{0.25}Ta_{0.75}S$/NF, respectively. The $Ni_{0.25}Nb_{0.75}S$/NF, $Ni_{0.25}Ta_{0.75}S$/NF and the activated products (CA-$Ni_{0.25}Nb_{0.75}S$/NF and CA-$Ni_{0.25}Ta_{0.75}S$/NF, respectively) maintain the Ni_3S_2 phase (Fig. 6a) due to the low metal doping degree (Nb of 0.44 atom % and Ta of 1.45 atom %) (Fig. S21a, b and Table S10). Besides, their nanocluster morphologies are also retained (Fig. S22). The Ni species are all reduced in CA-$Ni_{0.25}Nb_{0.75}S$/NF (Fig. 6b) and CA-$Ni_{0.25}Ta_{0.75}S$/NF (Fig. 6c) by XPS, accompanied by higher oxidation state of Nb(V) [50] (Fig. S21c) and Ta (V) [51] (Fig. S21d). These data confirm the similar modulation by the coupled tuning strategies. The HER polarization curves (Fig. 6d) display that CA-$Ni_{0.25}Nb_{0.75}S$/NF and CA-$Ni_{0.25}Ta_{0.75}S$/NF possess better HER activities than that of CA-NiS/NF. Hence it is concluded that the metal doping in the coupling strategies can be extended to more group VB metals.

Apart from sulfide species, the coupling tuning strategies can be applied to other Ni-based derivatives, such as nickel selenides ($Ni_{0.25}V_{0.75}Se$/NF, Figs. S23 and S24), phosphides ($Ni_{0.25}V_{0.75}P$/NF, Figs. S25 and S26) and oxides ($Ni_{0.25}V_{0.75}O$/NF, Figs. S27 and S28). The current densities (Figs. 7 and S29) of CA-$Ni_{0.25}V_{0.75}Se$/NF, CA-$Ni_{0.25}V_{0.75}P$/NF and CA-$Ni_{0.25}V_{0.75}O$/NF (at the overpotential of 300 mV) are expected to increase from 6.9, 39.6 and 2.8 to 104, 103 and 8.6 mA cm^{-2}, respectively, which is much superior to those of pristine catalysts. It undoubtedly confirm the versatility of coupled strategies of tuning the HER activity for higher catalytic performance in alkaline media.

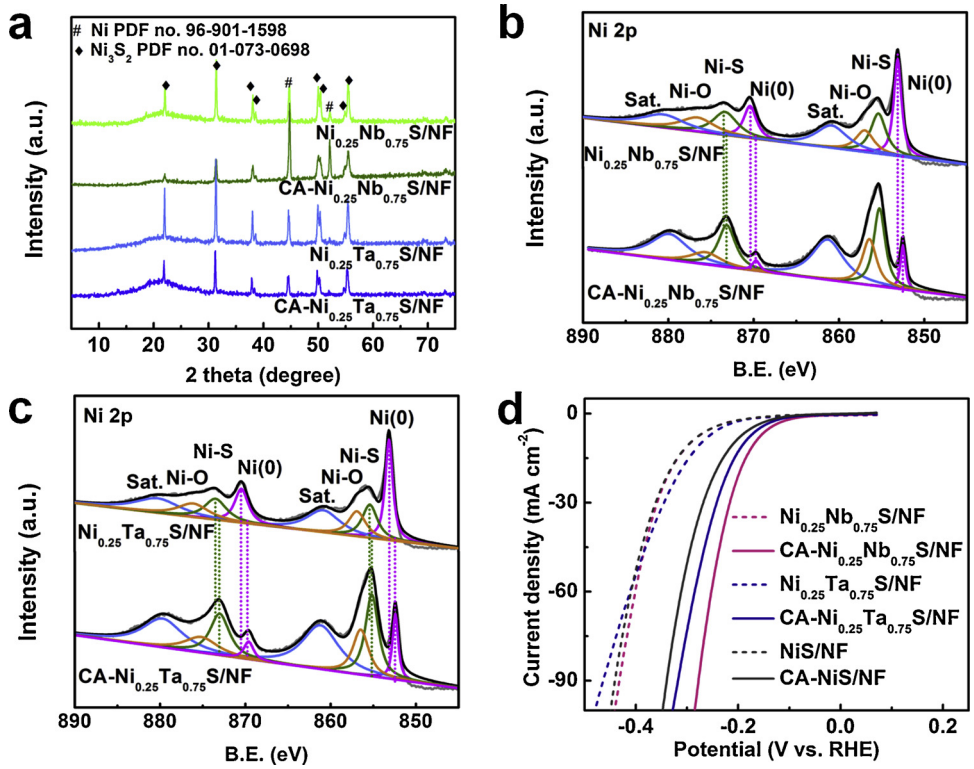

Fig. 6. XRD patterns of $Ni_{0.25}Nb_{0.75}S$/NF, CA-$Ni_{0.25}Nb_{0.75}S$/NF, $Ni_{0.25}Ta_{0.75}S$/NF and CA-$Ni_{0.25}Ta_{0.75}S$/NF. High-resolution XPS spectra of Ni 2p before and after ICA: (b) $Ni_{0.25}Nb_{0.75}S$/NF and (c) $Ni_{0.25}Ta_{0.75}S$/NF. (d) HER polarization curves of $Ni_{0.25}Nb_{0.75}S$/NF and $Ni_{0.25}Ta_{0.75}S$/NF before and after ICA.

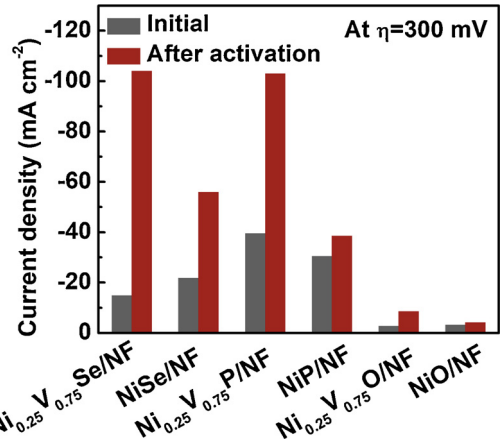

Fig. 7. Current densities at the overpotential of 300 mV before and after activation for $Ni_{0.25}V_{0.75}Se$/NF, $Ni_{0.25}V_{0.75}P$/NF and $Ni_{0.25}V_{0.75}O$/NF compared with pristine catalysts.

4. Conclusion

In summary, we systematically study the coupled tuning strategies involving group VB metal (V, Nb or Ta) doping and ICA to improve the alkaline HER performances on nickel-based materials (e.g., sulfides, selenides, phosphides and oxides) in alkaline media. For V-doped nickel sulfide, the bimetallic oxide-sulfide is constructed as the double-catalytic-site system. The ICA process induces the structure evolution to form the bimetallic oxide-sulfide hybrids, while V doping promotes the ICA process and optimizes the intrinsic ability of each site, indicating a strong coupling interaction between the tuning strategies. As a result, the activated catalyst achieves 4-fold higher intrinsic HER activity and 15-fold larger current density at the overpotential of 300 mV than those of pristine nickel sulfide. Our findings may provide a double-catalytic-site construction strategy for various nonprecious transition metal materials to achieve highly efficient water electrolysis.

Declaration of Competing Interest

The authors declare that they have no known competing financial interests or personal relationships that could have appeared to influence the work reported in this paper.

Acknowledgements

This work is financially supported by Major Program of Shandong Province Natural Science Foundation (ZR2018ZC0639) and the National Natural Science Foundation of China (21776314) and Shandong Provincial Natural Science Foundation (ZR2017MB059) and the Fundamental Research Funds for the Central Universities (18CX05016A).

Appendix A. Supplementary data

Supplementary material related to this article can be found, in the online version, at doi:https://doi.org/10.1016/j.apcatb.2019.117984.

References

[1] J.W. Ager, A.A. Lapkin, Chemical storage of renewable energy, Science 360 (2018) 707–708, https://doi.org/10.1126/science.aat7918.
[2] Z.W. Seh, J. Kibsgaard, C.F. Dickens, I. Chorkendorff, J.K. Norskov, T.F. Jaramillo, Combining theory and experiment in electrocatalysis: insights into materials design, Science 355 (2017), https://doi.org/10.1126/science.aad4998 eaad4998.
[3] J. Wei, M. Zhou, A. Long, Y. Xue, H. Liao, C. Wei, Z.J. Xu, Heterostructured electrocatalysts for hydrogen evolution reaction under alkaline conditions, Nano-Micro Lett. 10 (2018) 75, https://doi.org/10.1007/s40820-018-0229-x.
[4] C.F. Du, Q. Liang, R. Dangol, J. Zhao, H. Ren, S. Madhavi, Q. Yan, Layered trichalcogenidophosphate: a new catalyst family for water splitting, Nano-Micro Lett. 10 (2018) 67, https://doi.org/10.1007/s40820-018-0220-6.
[5] S. Anantharaj, S.R. Ede, K. Sakthikumar, K. Karthick, S. Mishra, S. Kundu, Recent trends and perspectives in electrochemical water splitting with an emphasis on sulfide, selenide, and phosphide catalysts of Fe, Co, and Ni: a review, ACS Catal. 6 (2016) 8069–8097, https://doi.org/10.1021/acscatal.6b02479.
[6] W. Liu, L. Zhang, T. Dong, H. Peng, Z. Wang, N. Zhang, X. Wang, P. Wu, Design of stable ultrasmall Pt-Ni(O) nanoparticles with enhanced catalytic performance: insights into the effects of Pt-Ni-NiO dual interfaces, ChemCatChem 10 (2018) 4134–4142, https://doi.org/10.1002/cctc.201800925.
[7] Y. Zheng, Y. Jiao, A. Vasileff, S.Z. Qiao, The hydrogen evolution reaction in alkaline solution: from theory, single crystal models, to practical electrocatalysts, Angew. Chem. Int. Ed. 57 (2017) 2–14, https://doi.org/10.1002/anie.201710556.
[8] B. Conway, B. Tilak, Interfacial processes involving electrocatalytic evolution and oxidation of H_2, and the role of chemisorbed H, Electrochim. Acta 47 (2002) 3571–3594, https://doi.org/10.1016/S0013-4686(02)00329-8.
[9] H. Liao, C. Wei, J. Wang, A. Fisher, T. Sritharan, Z. Feng, Z.J. Xu, A multisite strategy for enhancing the hydrogen evolution reaction on a nano-Pd surface in alkaline media, Adv. Energy Mater. 7 (2017), https://doi.org/10.1002/aenm.201701129 1701129.
[10] N. Danilovic, R. Subbaraman, D. Strmcnik, K.C. Chang, A. Paulikas, V. Stamenkovic, N.M. Markovic, Enhancing the alkaline hydrogen evolution reaction activity through the bifunctionality of $Ni(OH)_2$/metal catalysts, Angew. Chem. Int. Ed. 51 (2012) 12495–12498, https://doi.org/10.1002/anie.201204842.
[11] R. Subbaraman, D. Tripkovic, D. Strmcnik, K.-C. Chang, M. Uchimura, A.P. Paulikas, V. Stamenkovic, N.M. Markovic, Enhancing hydrogen evolution activity in water splitting by tailoring Li^+-Ni $(OH)_2$-Pt interfaces, Science 334 (2011) 1256–1260, https://doi.org/10.1126/science.1211934).
[12] Q. Xu, H. Jiang, H. Zhang, Y. Hu, C. Li, Heterogeneous interface engineered atomic configuration on ultrathin $Ni(OH)_2/Ni_3S_2$ nanoforests for efficient water splitting, Appl. Catal. B 242 (2019) 60–66, https://doi.org/10.1016/j.apcatb.2018.09.064.
[13] M. Gong, W. Zhou, M.-C. Tsai, J. Zhou, M. Guan, M.-C. Lin, B. Zhang, Y. Hu, D.-Y. Wang, J. Yang, Nanoscale nickel oxide/nickel heterostructures for active hydrogen evolution electrocatalysis, Nat. Commun. 5 (2014) 4695, https://doi.org/10.1038/ncomms5695.
[14] Q. Li, Z. Xing, D. Wang, X. Sun, X. Yang, In situ electrochemically activated CoMnS@NiO/CC nanosheets array for enhanced hydrogen evolution, ACS Catal. 6 (2016) 2797–2801, https://doi.org/10.1021/acscatal.6b00014.
[15] J. Zhang, T. Wang, P. Liu, S. Liu, R. Dong, X. Zhuang, M. Chen, X. Feng, Engineering water dissociation sites in MoS_2 nanosheets for accelerated electrocatalytic hydrogen production, Energy Environ. Sci. 9 (2016) 2789–2793, https://doi.org/10.1039/C6EE01786J.
[16] Y.F. Xu, M.R. Gao, Y.R. Zheng, J. Jiang, S.H. Yu, Nickel/nickel(II) oxide nanoparticles anchored onto cobalt(IV) diselenide nanobelts for the electrochemical production of hydrogen, Angew. Chem. Int. Ed. 52 (2013) 8546–8550, https://doi.org/10.1002/anie.201303495.
[17] N. Jiang, B. You, M. Sheng, Y. Sun, Electrodeposited cobalt-phosphorous-derived films as competent bifunctional catalysts for overall water splitting, Angew. Chem. Int. Ed. 54 (2015) 6251–6254, https://doi.org/10.1002/anie.201501616.
[18] C. Tang, H.F. Wang, Q. Zhang, Multiscale principles to boost reactivity in gas-involving energy electrocatalysis, Acc. Chem. Res. 51 (2018) 881–889, https://doi.org/10.1021/acs.accounts.7b00616.
[19] W. Chen, H. Wang, Y. Li, Y. Liu, J. Sun, S. Lee, J.S. Lee, Y. Cui, In situ electrochemical oxidation tuning of transition metal disulfides to oxides for enhanced water oxidation, ACS Cent. Sci. 1 (2015) 244–251, https://doi.org/10.1021/acscentsci.5b00227.
[20] C. Tsai, H. Li, S. Park, J. Park, H.S. Han, J.K. Norskov, X. Zheng, F. Abild-Pedersen, Electrochemical generation of sulfur vacancies in the basal plane of MoS_2 for hydrogen evolution, Nat. Commun. 8 (2017) 15113, https://doi.org/10.1038/ncomms15113.
[21] C. Yang, M. Gao, Q. Zhang, J. Zeng, X. Li, A. Abbott, In-situ activation of self-supported 3D hierarchically porous Ni_3S_2 films grown on nanoporous copper as excellent pH-universal electrocatalysts for hydrogen evolution reaction, Nano Energy 36 (2017) 85–94, https://doi.org/10.1016/j.nanoen.2017.04.032.
[22] Z. Lu, H. Wang, D. Kong, K. Yan, P.C. Hsu, G. Zheng, H. Yao, Z. Liang, X. Sun, Y. Cui, Electrochemical tuning of layered lithium transition metal oxides for improvement of oxygen evolution reaction, Nat. Commun. 5 (2014) 4345, https://doi.org/10.1038/ncomms5345.
[23] C. Hu, Q. Ma, S.-F. Hung, Z.-N. Chen, D. Ou, B. Ren, H.M. Chen, G. Fu, N. Zheng, In situ electrochemical production of ultrathin nickel nanosheets for hydrogen evolution electrocatalysis, Chem 3 (2017) 122–133, https://doi.org/10.1016/j.chempr.2017.05.011.
[24] F. Song, K. Schenk, X. Hu, A nanoporous oxygen evolution catalyst synthesized by selective electrochemical etching of perovskite hydroxide $CoSn(OH)_6$ nanocubes, Energy Environ. Sci. 9 (2016) 473–477, https://doi.org/10.1039/C5EE03453A.
[25] Z. Xiao, Y. Wang, Y.-C. Huang, Z. Wei, C.L. Dong, J. Ma, S. Shen, Y. Li, S. Wang, Filling the oxygen vacancies in Co_3O_4 with phosphorus: an ultra-efficient electrocatalyst for overall water splitting, Energy Environ. Sci. 10 (2017) 2563–2569, https://doi.org/10.1039/C7EE01917C.
[26] W. Gao, Z.D. Hood, M. Chi, Interfaces in heterogeneous catalysts: advancing mechanistic understanding through atomic-scale measurements, Acc. Chem. Res. 50 (2017) 787–795, https://doi.org/10.1021/acs.accounts.6b00596.
[27] B. Zhang, X. Ye, W. Dai, W. Hou, Y. Xie, Biomolecule assisted synthesis and electrochemical hydrogen storage of porous spongelike Ni_3S_2 nanostructures grown directly on nickel foils, Chem-Eur J. 12 (2006) 2337–2342, https://doi.org/10.

1002/chem.200501005).
[28] J. Jiang, A. Zhang, L. Li, L. Ai, Nickel–cobalt layered double hydroxide nanosheets as high-performance electrocatalyst for oxygen evolution reaction, J. Power Sources 278 (2015) 445–451, https://doi.org/10.1016/j.jpowsour.2014.12.085.
[29] N. Jiang, L. Bogoev, M. Popova, S. Gul, J. Yano, Y. Sun, Electrodeposited nickel-sulfide films as competent hydrogen evolution catalysts in neutral water, J. Mater. Chem. A 2 (2014) 19407–19414, https://doi.org/10.1039/C4TA04339A.
[30] K. Fan, H. Chen, Y. Ji, H. Huang, P.M. Claesson, Q. Daniel, B. Philippe, H. Rensmo, F. Li, Y. Luo, L. Sun, Nickel-vanadium monolayer double hydroxide for efficient electrochemical water oxidation, Nat. Commun. 7 (2016) 11981, https://doi.org/10.1038/ncomms11981.
[31] N. Cheng, Q. Liu, A.M. Asiri, W. Xing, X. Sun, A Fe-doped Ni_3S_2 particle film as a high-efficiency robust oxygen evolution electrode with very high current density, J. Mater. Chem. A 3 (2015) 23207–23212, https://doi.org/10.1039/C5TA06788J.
[32] H. Liang, H. Shi, D. Zhang, F. Ming, R. Wang, J. Zhuo, Z. Wang, Solution growth of vertical VS_2 nanoplate arrays for electrocatalytic hydrogen evolution, Chem. Mater. 28 (2016) 5587–5591, https://doi.org/10.1021/acs.chemmater.6b01963.
[33] Z. Liang, H.S. Ahn, A.J. Bard, A study of the mechanism of the hydrogen evolution reaction on nickel by surface interrogation scanning electrochemical microscopy, J. Am. Chem. Soc. 139 (2017) 4854–4858, https://doi.org/10.1021/jacs.7b00279.
[34] Q. Ma, C. Hu, K. Liu, S.-F. Hung, D. Ou, H.M. Chen, G. Fu, N. Zheng, Identifying the electrocatalytic sites of nickel disulfide in alkaline hydrogen evolution reaction, Nano Energy 41 (2017) 148–153, https://doi.org/10.1016/j.nanoen.2017.09.036.
[35] Y. Mu, F. Jia, Z. Ai, L. Zhang, Iron oxide shell mediated environmental remediation properties of nano zero-valent iron, Environ. Sci. Nano 4 (2017) 27–45, https://doi.org/10.1039/C6EN00398B.
[36] X. Zou, Y. Wu, Y. Liu, D. Liu, W. Li, L. Gu, H. Liu, P. Wang, L. Sun, Y. Zhang, In situ generation of bifunctional, efficient Fe-based catalysts from mackinawite iron sulfide for water splitting, Chem 4 (2018) 1139–1152, https://doi.org/10.1016/j.chempr.2018.02.023.
[37] C.G. Morales-Guio, L.A. Stern, X. Hu, Nanostructured hydrotreating catalysts for electrochemical hydrogen evolution, Chem. Soc. Rev. 43 (2014) 6555–6569, https://doi.org/10.1039/C3CS60468C.
[38] S. Anantharaj, S. Ede, K. Karthick, S.S. Sankar, K. Sangeetha, P. Karthik, S. Kundu, Precision and correctness in the evaluation of electrocatalytic water splitting: revisiting activity parameters with a critical assessment, Energy Environ. Sci. 11 (2018) 744–771, https://doi.org/10.1039/C7EE03457A.
[39] W.-F. Chen, C.-H. Wang, K. Sasaki, N. Marinkovic, W. Xu, J. Muckerman, Y. Zhu, R. Adzic, Highly active and durable nanostructured molybdenum carbide electrocatalysts for hydrogen production, Energy Environ. Sci. 6 (2013) 943–951, https://doi.org/10.1039/C2EE23891H.
[40] M. Asnavandi, C. Zhao, Autologous growth of nickel oxyhydroxides with in situ electrochemical iron doping for efficient oxygen evolution reactions, Mater. Chem. Front. 1 (2017) 2541–2546, https://doi.org/10.1039/C7QM00367F.
[41] J. van Drunen, B. Kinkead, M.C. Wang, E. Sourty, B.D. Gates, G. Jerkiewicz, Comprehensive structural, surface-chemical and electrochemical characterization of nickel-based metallic foams, ACS Appl. Mater. Interfaces 5 (2013) 6712–6722, https://doi.org/10.1021/am401606n.
[42] L.L. Feng, G. Yu, Y. Wu, G.D. Li, H. Li, Y. Sun, T. Asefa, W. Chen, X. Zou, High-index faceted Ni_3S_2 nanosheet arrays as highly active and ultrastable electrocatalysts for water splitting, J. Am. Chem. Soc. 137 (2015) 14023–14026, https://doi.org/10.1021/jacs.5b08186.
[43] Y. Deng, L.R.L. Ting, P.H.L. Neo, Y.-J. Zhang, A.A. Peterson, B.S. Yeo, Operando Raman spectroscopy of amorphous molybdenum sulfide (MoS_x) during the electrochemical hydrogen evolution reaction: identification of sulfur atoms as catalytically active sites for H+ reduction, ACS Catal. 6 (2016) 7790–7798, https://doi.org/10.1021/acscatal.6b01848.
[44] J.X. Feng, J.Q. Wu, Y.X. Tong, G.R. Li, Efficient hydrogen evolution on Cu nanodots-decorated Ni_3S_2 nanotubes by optimizing atomic hydrogen adsorption and desorption, J. Am. Chem. Soc. 140 (2018) 610–617, https://doi.org/10.1021/jacs.7b08521.
[45] N.K. Chaudhari, H. Jin, B. Kim, K. Lee, Nanostructured materials on 3D nickel foam as electrocatalysts for water splitting, Nanoscale 9 (2017) 12231–12247, https://doi.org/10.1039/C7NR04187J.
[46] J. Liu, D. Zhu, Y. Zheng, A. Vasileff, S.-Z. Qiao, Self-supported earth-abundant nanoarrays as efficient and robust electrocatalysts for energy-related reactions, ACS Catal. 8 (2018) 6707–6732, https://doi.org/10.1021/acscatal.8b01715.
[47] C. Xiao, Y. Li, X. Lu, C. Zhao, Bifunctional porous NiFe/$NiCo_2O_4$/Ni foam electrodes with triple hierarchy and double synergies for efficient whole cell water splitting, Adv. Funct. Mater. 26 (2016) 3515–3523, https://doi.org/10.1002/adfm.201505302.
[48] W. Zhu, R. Zhang, F. Qu, A.M. Asiri, X. Sun, Design and application of foams for electrocatalysis, ChemCatChem 9 (2017) 1721–1743, https://doi.org/10.1002/cctc.201601607.
[49] W. Chen, H. Wang, Y. Li, Y. Liu, J. Sun, S. Lee, J.-S. Lee, Y. Cui, In situ electrochemical oxidation tuning of transition metal disulfides to oxides for enhanced water oxidation, ACS Cent. Sci. 1 (2015) 244–251, https://doi.org/10.1021/acscentsci.5b00227.
[50] A.K. Kulkarni, C. Praveen, Y.A. Sethi, R.P. Panmand, S.S. Arbuj, S.D. Naik, A.V. Ghule, B.B. Kale, Nanostructured N-doped orthorhombic Nb_2O_5 as an efficient stable photocatalyst for hydrogen generation under visible light, Dalton Trans. 46 (2017) 14859–14868, https://doi.org/10.1039/C7DT02611K.
[51] Z. Awaludin, T. Okajima, T. Ohsaka, Electroreduced tantalum pentaoxide for hydrogen evolution reaction, Chem. Lett. 43 (2014) 1248–1250, https://doi.org/10.1246/cl.140312.